Computational and Structural Biotechnology Journal 19 (2021) 2236–2245

COMPUTATIONAL AND STRUCTURAL BIOTECHNOLOGY JOURNAL

journal homepage: www.elsevier.com/locate/csbj

Spatial topological analysis of sympathetic neurovascular characteristic of acupoints in Ren meridian using advanced tissue-clearing and near infrared II imaging

Wei Hu [a,b,1], Junda Chen [c,g,1], Caixia Sun [d,1], Xiaoyu Tong [a,b], Wenhan Lu [a,b], Ziyong Ju [e], Yong Xia [e], Zhenle Pei [a,b], Mingzhen Xu [a,b], Xiaoqing Xu [a,b], Jiemei Shi [a,b], Yi Li [e], Haofeng Chen [a,b], Yizhou Lu [a,b], Ying Ying [a,b], Hongru Gao [a,b], Aaron J.W. Hsueh [f], Fan Zhang [d], Zhi Lü [g,*], Yi Feng [a,b,*]

[a] *Department of Integrative Medicine and Neurobiology, School of Basic Medical Sciences, Institutes of Brain Science, Brain Science Collaborative Innovation Center, State Key Laboratory of Medical Neurobiology, Institute of Acupuncture and Moxibustion, Fudan Institutes of Integrative Medicine, Fudan University, Shanghai 200032, China*
[b] *Shanghai Key Laboratory of Acupuncture Mechanism and Acupoint Function, Shanghai 200032, China*
[c] *School of Mathematical Sciences, East China Normal University, Shanghai 200241, China*
[d] *Department of Chemistry, Shanghai Key Laboratory of Molecular Catalysis and Innovative Materials, State Key Laboratory of Molecular Engineering of Polymers and iChem, Fudan University, Shanghai 200433, China*
[e] *Department of Acupuncture and Tuina, Shanghai University of Traditional Chinese Medicine, Shanghai 201203, China*
[f] *Division of Reproductive and Stem Cell Biology, Departments of Obstetrics and Gynecology, School of Medicine, Stanford University, CA 94305, USA*
[g] *School of Mathematical Sciences, Fudan University, Shanghai 200433, China*

ARTICLE INFO

Article history:
Received 13 January 2021
Received in revised form 2 April 2021
Accepted 3 April 2021
Available online 08 April 2021

Keywords:
Acupuncture
Acupoint
Tissue-clearing
3D visualization
Topology
In-vivo NIR-II imaging

ABSTRACT

Acupuncture has been used for treating various medical conditions in traditional Chinese medicine. Both manual and electro-acupuncture stimulate specific acupoints to obtain local and systemic biological effects, but the underlying mechanisms remain unclear. Here, we used three-dimensional tissue-clearing technology to study acupoints on the Ren meridian of mice to reveal the distribution, density, branching, and relationships between blood vessels and nerves. Using topological *Mapper* methods, we found that sympathetic neurovascular networks were denser in the CV 4 acupoint compared with surrounding non-acupoints. Furthermore, high resolution *in vivo* real-time vascular imaging using the near infrared-II probe LZ-1105 demonstrated increased blood flow in the CV 4 acupoint compared with neighboring non-acupoints after manual or electro-acupuncture. Consistent with earlier findings, our research indicated that acupuncture could enhance local blood flow, and our high-resolution 3D images show for the first time the important role of sympathetic neurovascular networks in the CV 4 acupoint.

1. Introduction

Acupuncture, with a history of over 2000 years, is an important part of traditional Chinese medicine, and in modern times both manual acupuncture (MA) and electroacupuncture (EA) are used for stimulation of acupoints [1]. There are 361 accepted acupoints distributed along 12 main meridians [2,3], and selection of the appropriate acupoints for acupuncture has been appreciated by physicians of traditional Chinese medicine as an effective method for treating various diseases. CV 4 (Guanyuan), for example, is a commonly used acupoint for the treatment of genitourinary disorders such as infertility, dysmenorrhea, polycystic ovarian syndrome, premature ovarian failure, and urinary retention [4-9].

Much effort has been put into identifying the superficial, middle, and deep layers of acupoints [10], together with surrounding blood vessels, nerves, connective tissues, and immune cells [11]. Considering the comprehensive and bilateral fine regulation of acupuncture, the neuro–endocrine–immune (NEI) network might better explain the complex mechanism behind acupuncture's effects [12–14]. Acupuncture might cause amplified signal transmission through the NEI cascade, such as neuropeptides, hormones, and inflammatory factors. Such cascades begin within the acupoint microenvironment, spread through the meridian network

* Corresponding authors at: P.O. Box 291, 138 Yi-Xue-Yuan Road, Shanghai 200032, China (Y. Feng). P.O. School of Mathematical Sciences, Fudan University, 220 Handan Road, Shanghai, 200433, P.R. China. Tel: 86-21-5566-5005, Fax: 86-21-5566-5005 (Z. Lü).
E-mail addresses: zlu@fudan.edu.cn (Z. Lü), fengyi17@fudan.edu.cn (Y. Feng).
[1] These authors contributed equally.

https://doi.org/10.1016/j.csbj.2021.04.010

regulated by the NEI, and end with an effect on the target organs [14,15]. Using computed tomography, dense micro-vessels were found in acupoints [16,17], while histochemical staining revealed dense nerve bundles in acupoints [18–20]. However, the exact relationships among these neurovascular components are unclear [21].

Acupoints corresponding to those in humans have been identified in mice and rats [22,23], thus providing a basis for in-vitro and in-vivo analyses using animal models. Tissue-clearing is an emerging method to render large piece of tissue or intact organs transparent, thus allowing for 3D single-cell imaging without structural damage [24–26]. Furthermore, recently developed noninvasive fluorescence imaging in the near-infrared two (NIR-II, 1000–1700 nm) wavelength region has allowed deeper tissue penetration *in vivo*, longer observation time, higher resolution, and lower background, thus providing the basis for investigating real-time blood flow changes in live animals [27–29].

In this work, three-dimensional visualization of neurovascular networks in the CV 4 acupoint at the Ren meridian using both in vitro and *in vivo* real-time monitoring of blood flow before and after acupuncture provides further understanding of the molecular basis of the Ren meridian.

2. Materials and methods

All the reagents, antibodies, equipment, and software used in the experiments are listed in the Supplementary table 1.

Animals and ethics

The current study was approved by the Animal Ethics Committee of Shanghai Medical College, Fudan University, Shanghai, China (ID:20160225-013 and 20200306-004). Twenty-six adult female nude mice and 21 C57B/6 mice were purchased from Shanghai Laboratory Animal Center (SLAC) (Shanghai, China). The mice were housed at 5 or 6 animals per cage under controlled standard conditions (21–23 °C, 34–40% humidity, and a 12 h light/12 h dark cycle). All the mice had free access to tap water, and they were fed the same standard laboratory chow (SLAC, Shanghai, China). Twenty-six nude mice were randomly divided into two groups, and eight were used for the in vitro CUBIC experiment while 18 were used for the *in vivo* NIR-II experiment (Fig. 1). For the CUBIC experiment, mice were assigned to the control group and the EA group (n = 4). In the *in vivo* NIR-II experiment, 18 mice were evenly and randomly distributed into the control, MA, and EA groups (n = 6). The twenty-one C57B/6 mice were randomly divided into the control (n = 7), ovariectomy (OVX, n = 7), and ovariectomy with EA (OVX + EA, n = 7) groups.

MA and EA treatment

MA and EA treatments were given by professional acupuncturists, and MA served as sham EA. The mice were anesthetized with isoflurane (4 ml/min, R510-22–16, Shenzhen RWD Life Science Co., Ltd) using an animal anesthesia device (RMAS-100921001, Raymain Instrument Co., Ltd., China). The acupuncture needle (0.3 mm × 25 mm; Suzhou Acupuncture Goods Co., Ltd, China) was inserted into CV 4, located at the point about 6 mm from the navel (three fifths of the length from the navel to the pubic symphysis in the linea alba). For the MA group, the needle remained superficially inserted in CV 4, while for the EA group electrical stimulation of 0.8–1.4 mA at 2 Hz was applied to the 1 mm deep needles with an electrical stimulator (HANS-LH202, Huawei Co., Ltd., Beijing, China) and a reference electrode in the tail forming a current loop [30,31]. The electrical intensity was adjusted based on the tolerance of the mouse, and each treatment lasted for 30 min.

Ren meridian tissue collection and the CUBIC process

The CUBIC process was performed according to the protocol of Susaki et al. [32]. Briefly, mice were intracardially perfused with 20 ml 1 × phosphate-buffered saline (PBS) at 4 °C containing 10 U/ml of heparin to wash out the blood, followed by the same volume of 4% paraformaldehyde (PFA) at 4 °C. The mouse Ren meridian was dissected out along the linea alba of the abdomen, extending from the navel to the pubic symphysis, together with the skin, subcutaneous tissue, and muscle. Dissected samples were immersed in 4% PFA at 4 °C for 24 h. Before clearing, samples were pre-treated by washing with 1 × PBS/0.01% sodium azide (SA) for 2–4 h at 37 °C on a shaker to remove the PFA. All the CUBIC clearing steps were conducted at 37 °C on the shaker. Samples were first washed with 50% diluted CUBIC clearing solution (25% urea, 25% tetraethylenediamine, 15% Triton X-100) for 3 h and then incubated with 100% clearing solution for 3 days until turning transparent. After washing with 1 × PBS/0.01% SA for 2 h three times, the samples underwent immunofluorescence staining. The samples were then washed with 50% diluted Scale solution (25% urea, 50% sucrose, 10% triethanolamine) for about 12 h until the samples sank to the bottom of the container. This was followed by immersing the samples in 100% Scale solution for at least 1 day until they turned completely transparent.

Immunofluorescence staining

Transparent tissue samples were washed in 1 × PBS/0.01% SA for 24 h and then incubated with primary antibodies against tyrosine hydroxylase (1:50, rabbit polyclonal to tyrosine hydroxylase, ab112, Abcam) or platelet endothelial cell adhesion molecule/CD31 (1:10, rabbit polyclonal to CD31, ab28364, Abcam) dissolved in 1 × PBS/0.01% SA for 48 h, followed by washing in 1 × PBS/0.01% SA for 24 h. Samples were then incubated with the secondary antibody (1:100, Alexa 488 anti-rabbit, A11034, Life Technologies or 1:100, Alexa-594 anti-rabbit, A11012, Life Technologies), lectin dye (1:100, Tomato, 594DL-1177, DyLight), and 4′,6-diamidino-2-phenylindole (1:100, DAPI, D9542, Sigma-Aldrich), which were all dissolved in 1 × PBS/0.01% SA, and incubated for 48 h covered by aluminum foil to avoid fluorescence bleaching. Finally, all samples were washed with 1 × PBS/0.01% SA buffer for 24 h.

Lightsheet imaging and image analysis

The lightsheet microscope (Lightsheet Z.1, Zeiss, 5X, German) was used to image the intact transparent samples, and Imaris software (Imaris 9.5, Oxford Instruments PLC, UK) was used to perform the 3D analysis of the obtained images. Several algorithms in the Imaris software were used in this research, including *Filament, Surface, Coloc*. The *Filament* algorithm was used for tracing nerves and vessels and for identifying branching, while the *Surface* algorithm was used for reconstructing irregular morphologies and for calculating volumes. The *Coloc* algorithm was used to analyze the overlap between two selected channels. "*Vessel/Nerve Diameter*" was automatically calculated after tracing with *Filament*, and "*Vessel/Nerve density*" was calculated as the number of vessels/nerves divided by tissue volume, where the number was automatically calculated by *Filament* and the volume was automatically calculated by *Surface*. "*Capillary branching density*" was calculated as the number of vessels with branching

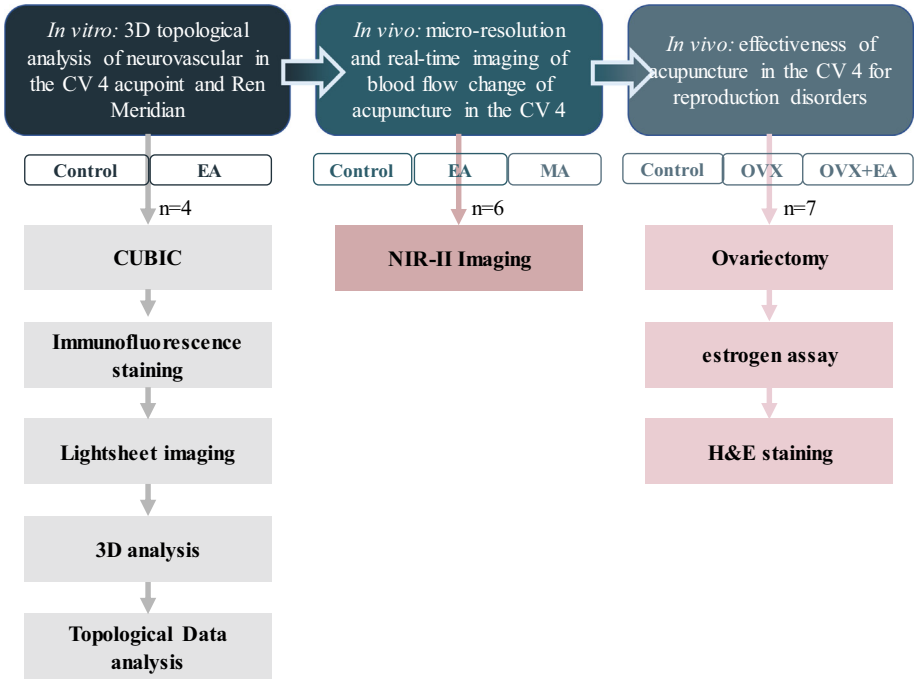

Fig. 1. Experimental methodology flow. EA, electroacupuncture; MA, manual electroacupuncture; OVX, ovariectomy; CUBIC, clear, unobstructed brain/body imaging cocktails and computational analysis; H&E staining, hematoxylin and eosin staining.

divided by the total number of vessels, where both numbers were automatically calculated after tracing with *Filament*. *"Overlap between vessel and nerve"* was automatically calculated by *Coloc*, which was set to calculate the overlap between the channels for vessels and nerves.

Topological data analysis

Original data was obtained from the *Filament* algorithm in *Imaris* after reconstruction of the original lightsheet imaging data. *Mapper* is a computation tool for topological data analysis that is used to extract key 3D information such as intensity, localization, colonization, etc., and to re-express it in 2D form [33]. The first step is to choose a proper filter (a function mapped to a real number or higher-dimensional Euclidean space). The second step is to divide the value of the filter into certain intervals (the value of filter is shown by the color of the node). According to the needs of the situation, if a finer structure is required then the segmentation is finer. The third step is to cluster the pre-images of each interval, and the fourth step is to make the final connection graph (every clustered class is shown as a node in the results, and the number of nodes shows how much data it contains). If the intersection between two classes is not empty, then these two classes are connected by a line. The more branching points, the looser the internal structure connection.

NIR-II imaging

All the NIR-II imaging was conducted according to the protocol of Li et al. [34]. LZ-1105 was used as the molecular dye for NIR-II imaging because its absorption and emission wavelength are beyond 1000 nm and because of its long blood circulation time (half-life of 3.2 h). Briefly, mice were anaesthetized with 2% sodium pentobarbital (30 mg/kg, P-3761, Sigma-Aldrich, USA) and intravenously injected with LZ-1105 (5 mg/kg, 25-gauge needle) in the tail at the beginning of the experiment. A 640 × 512 pixel InGaAs NIRvana640LN camera and a home-built InGaAs array detector (Princeton Instruments NIRvana640LN) was used to collect all of the NIR-II images. The excitation laser was a 1064 nm laser diode at a power density of ~70 mW/cm^2 (lower than the safe exposure limit of 1.0 W/cm^2 as determined by the International Commission on Nonionizing Radiation Protection), and the emission was collected with a 1,400 nm long-pass filter (FEL1400,Thorlabs, Inc., USA). Throughout the imaging process, the mouse was fixed on a stable stage. Images and movies were processed with the LightField imaging software (v6.11, Teledyne Digital Imaging, USA) and MATLAB (R2015b, MathWorks, USA). The exposure time for all images was 300 ms.

Ovariectomy, estrogen assay, and uterine histology and morphometry

The OVX and OVX + EA groups underwent bilateral ovariectomy after isoflurane anesthesia. Bilateral ovaries were ligated and dissected following the protocol of Souza et al.[35]. The control group underwent sham surgery, and only a small amount of fat tissue around the ovaries was dissected out. After surgery, daily intramuscular injection of penicillin (2,500 U) was administered for 3 days. Two weeks after ovariectomy, mice in the OVX + EA group received 3 days of EA treatment. Estrogen was assayed with enzyme-linked immunosorbent assay (ELISA) kit (Beijing Sino-UK Institute of Biological Technology) following the manufacturer's protocol.

For uterine histology and morphometry, each uterus was dissected completely from the junction of the cervix, and uterine weight was recorded after removing the peripheral fat and excess fluid. The uterus was then kept in 4% PFA at room temperature for 24 h, embedded in paraffin, and sectioned at a thickness of 5 μm followed by hematoxylin and eosin staining (Thermo Fisher Scientific, USA).

10.1. Statistical analysis

All data were analyzed by GraphPad Prism (v 8.0.2, GraphPad Software, Inc., San Diego, CA, USA) and are presented as means ± standard errors. Using the Shapiro–Wilk test, the distributions were first tested for all the datasets and shown to be normally distributed. One-way ANOVA and Dunnett's comparison were performed to calculate the significance between the groups, and two-way ANOVA was used to compare the groups when examining two independent variables. $P < 0.05$ was set as the limit for statistical significance.

11. Results

11.1. 3D neurovascular architecture in acupoints and non-acupoints

To explore the 3D neurovascular structures of acupoints, part of the Ren meridian extending from CV 3 to CV 7 was dissected out and cleared by CUBIC for large-tissue 3D imaging (Fig. 2a). Using the linea alba and inferior abdominal vessels as anatomic landmarks, CV 3 (Zhongji), CV 4 (Guanyuan), CV 5 (Shimen), and CV 7 (Yinjiao) were found to be located at four quintile points with a distance between them of about 2,000 μm along the linea alba in the middle of two inferior abdominal vessels (Supplementary video 1). A square area of 500 μm × 500 μm was defined as an acupoint, and four equal-size areas located about 1000 mm away from CV 4 in the up, down, left, and right directions were defined as non-acupoints, where the 1000 mm distance from the CV 4 was just at the mid-point between two acupoints on the Ren meridian (Fig. 2b). The 3D structures of the acupoints were stratified and divided into skin and muscle layers. Based on the positional relationship between the neurovascular network and muscle fibers, the muscle layer was further sub-divided into two groups, one parallel to the muscle fibers and the other almost perpendicular to the muscle fibers. The muscle-parallel neurovasculature consisted of capillaries and parallel nerves, and the perpendicular neurovasculature consisted of perpendicular vessels and perpendicular nerves (Fig. 2c, Supplementary video 2).

Denser sympathetic neurovascular networks in the CV 4 acupoint compared with the neighboring non-acupoints

According to the classification described above, the 3D neurovasculatures were constructed for CV 4 and the surrounding non-acupoints including CV 4-U (up), CV 4-D (down), CV 4-L (left), and CV 4-R (right) (Fig. 3a-c). The spatial parameters of vessels, including density, diameter, and branching density, were calculated. Although there were no changes in diameters of vessels and nerves, there was a small change in capillary density in the muscle layer (Supplementary Fig. 1a). Interestingly, the capillary branching density was much higher in acupoints as compared to non-acupoints (Fig. 3d, e). Furthermore, ratios of overlapping between nerves and vessels were higher in CV 4 compared to non-acupoints (Fig. 3f, g).

Topologic analysis showing fewer neurovascular branching points at acupoints

The spatial features of the reconstructed neurovascular 3D structures centered in the CV 4 acupoints were further analyzed using topological methods. First, plotting the 3D vascular structures of CV 3–7 and mapping their skeletons revealed branching points that could affect the efficiency of the blood flow [36,37] (Fig. 4 for CV 4 and supplementary Fig. 4 for CV 3, 5, 7). We traced vessels centered in CV 4 (Fig. 4a) and mapped the vasculature of both acupoints and non-acupoints in order to explore the continuity between acupoints and non-acupoints (Fig. 4b). We further plotted vessel branching point and vessel length, and as shown in Fig. 4c the acupoint showed fewer branching points and longer vessel length compared with non-acupoints. Moreover, the *Mapper* algorithm was used to further analyze the branching points of sympathetic neurovascular networks in CV 4 and surrounding non-acupoints. As shown in Fig. 4d, different levels of branching points could be found. Similar to the vasculature, the neurovascular network showed fewer branching points in acupoints (Fig. 4e).

EA increased blood flow in CV 4 but not in the surrounding non-acupoints

To investigate if the observed sympathetic neurovascular network could lead to blood flow changes after the stimulation of the acupoints, we further compared the blood flow differences between CV 4 and its surrounding non-acupoints *in vivo*. Using NIR-II real-time imaging, we quantitatively recorded the blood flow changes induced by MA or EA (Fig. 5a). Both MA and EA induced gradual increases in blood flow in CV 4 during the 30 min treatment, with EA being more effective than MA. After the 30 min treatment period, the blood flow induced by EA lasted longer than MA (Supplementary Fig. 5b-c). In contrast, the blood flow in the non-acupoints surrounding CV 4 did not show any changes during the whole recording period (Fig. 5b-c dashed lines).

15. Discussion

In the present study, we first performed the tissue-clearing CUBIC method to make the Ren meridian samples completely transparent, and then we reconstructed the 3D neurovascular structure of acupoints CV 3–7. According to the histological stratification and spatial position in relation to the muscle fibers, we defined a novel classification model for the neurovascular 3D structure that formed the basis for our further quantitative and statistical analysis. In our model, we collected the data in a cuboid with a length and width of 500 μm surrounding acupoints CV 3–7 in order to compare the variations among them. Considering the diameter of the acupuncture needle (0.12 ~ 0.25 mm) [38], we chose 500 μm to make sure including the whole acupoint area. We found the capillary branching and sympathetic neurovascular networks of CV 4 to be significantly denser compared with the surrounding non-acupoints. *Mapper*, an analytical method for high-dimensional data, was used to estimate the topological features of the sympathetic neurovascular networks in CV 4. The observed amplification structures were consistent with the *in vivo* NIR-II results in which EA and MA induced more intense blood flow in CV 4 compared with the surrounding non-acupoints. In our study, EA of CV 4 could improve the reproductive endocrine function in ovariectomized mice, as manifested by elevated estrogen levels, and could improve the uterine morphology, which reflected the comprehensive regulatory effects of acupuncture (Supplementary Fig.6).

Numerous theories have been put forth to explain the mechanism of acupuncture [21,39]. The nervous system, especially the peripheral nervous system, has long been thought to be the main basis for acupuncture's effects [40]. Multiple nerve endings and specialized receptors accumulate in acupoints, which form the complex afferent sensory system [41]. Regulation of the internal viscera is mediated by the autonomic nervous system (ANS), and acupuncture might influence ANS regulation patterns through stimulation of the neurovascular structures of acupoints, especially the sympathetic nervous system [12,42,43]. This visceral connection is widely used to manage visceral diseases in the clinic [44].

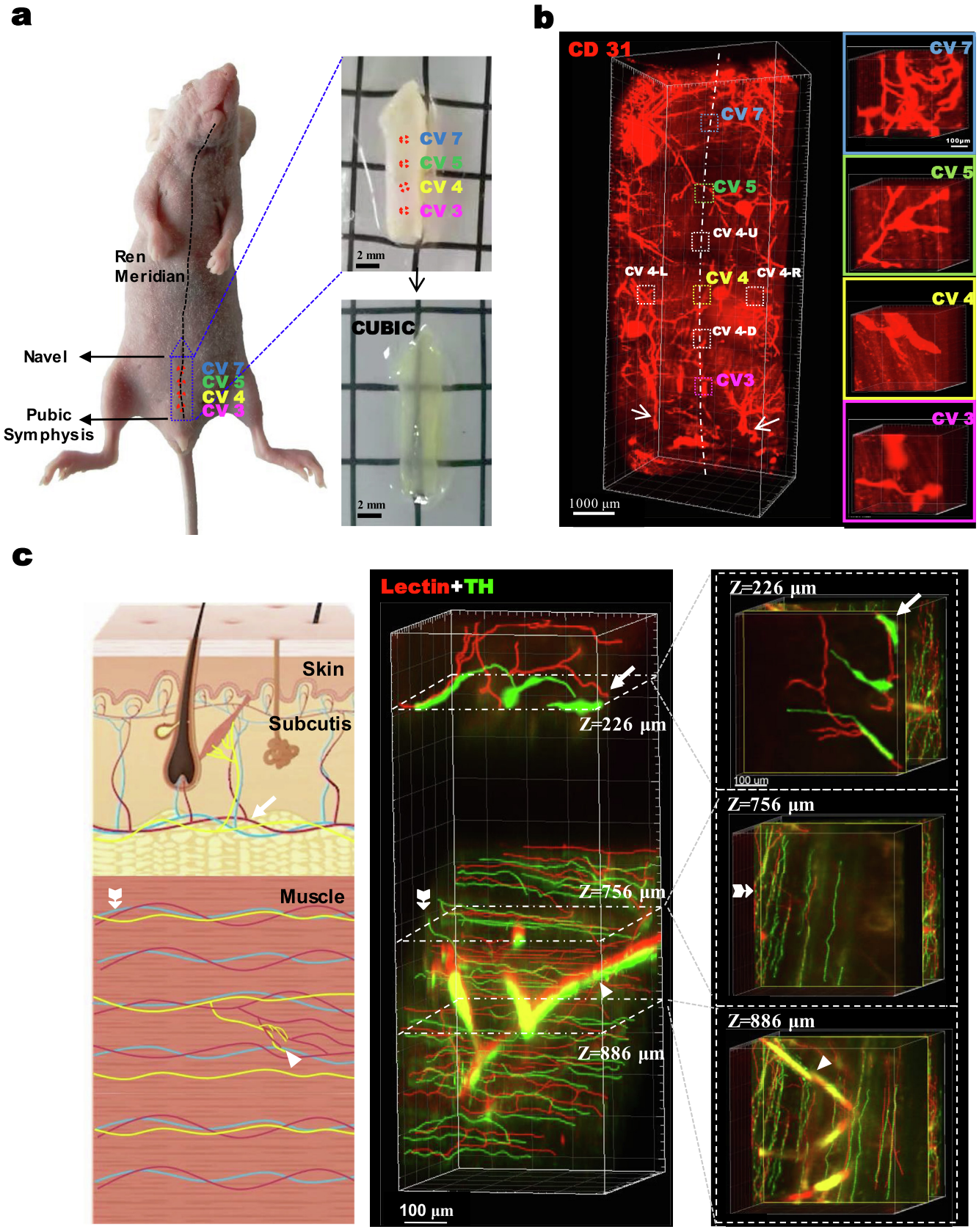

Fig. 2. The location and stratification of the neurovascular 3D structure of acupoints and surrounding non-acupoints from a randomly chosen mouse a). Location, sampling, and CUBIC treatment of Ren meridian tissues consisting of CV 3, 4, 5, and 7. b). 3D structure of the vasculature in the Ren meridian highlighting acupoints and non-acupoints. The anatomic landmarks of the linea alba and the two IAVs (inferior abdominal vessels) are shown as the white dashed line and arrows, respectively. Insets show enlarged acupoints with vessels and capillaries. c). The stratified neurovascular 3D structure of CV 4. Left panel: Acupoints could be divided into the upper skin layer and lower muscle layer. Middle panel: Blood vessels (Red) and sympathetic nerves (Green) were identified. The upper skin layer consisted of non-parallel and non-intermingled nerves and vessels. The lower muscle layer could be divided into the upper region with parallel vessels and nerves, whereas the lower region had perpendicular vessels and nerves. Right panel: Horizontal view of the neurovascular relationships at different depths. Thin arrows: vessels and nerves in the skin layer. Thick arrows: parallel capillaries and nerves in the upper region of muscle. Arrowhead: perpendicular vessels and nerves in the lower muscle layer. (For interpretation of the references to color in this figure legend, the reader is referred to the web version of this article.)

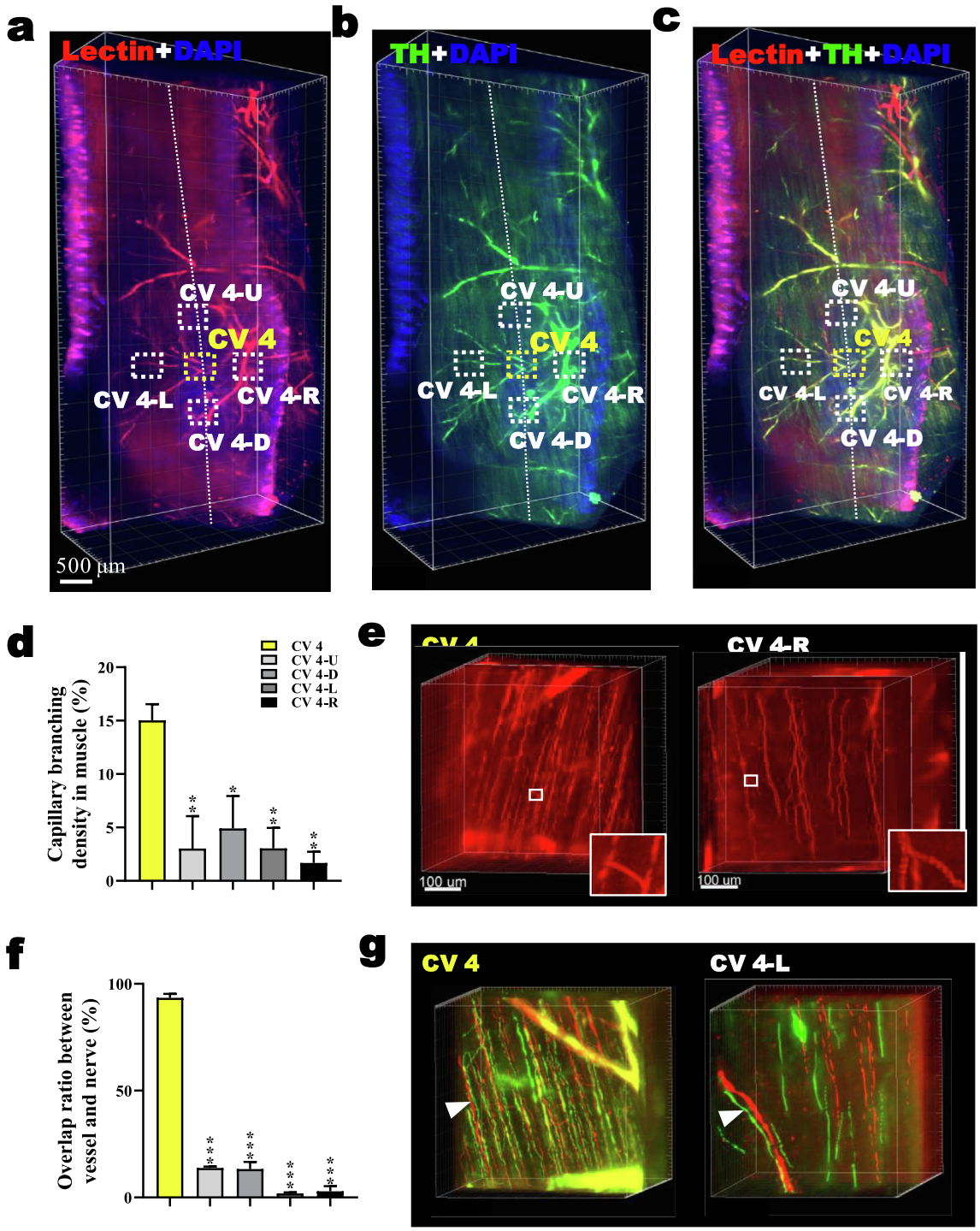

Fig. 3. Denser sympathetic neurovascular networks in the CV 4 acupoint compared with the neighboring non-acupoints 3D structure of CV 4 and surrounding non-acupoints showing a) vascular networks (red, lectin; blue, DAPI), b) neural networks (green, TH; blue, DAPI), and c) merged staining. d). Denser capillary branching in CV 4 compared with surrounding non-acupoints. e). Representative graphs showing vascular staining in CV 4 and CV 4-R. Capillary branching density in muscle = number of vessels with branching/total number of vessels f). Ratio of overlapping vessels and nerves. g). representative graphs showing denser neurovascular networks in CV4 compared to CV 4-L. n = 4/group, *p < 0.05, **p < 0.01, ***p < 0.001. (For interpretation of the references to color in this figure legend, the reader is referred to the web version of this article.)

In our work, we found that topologically reduced branching and enriched sympathetic neurovascular interactions might form the structural basis of the acupoint, thus revealing the important role of the ANS in acupuncture.

Acupoints are rich in vessels and nerve endings, but due to the limitations of gross anatomy and pathological sections, neurovascular 3D structures have been difficult to observe. In our present study, we used the CUBIC method to completely preserve the skin, subcutaneous tissue, and muscles together with the 3D interspersed vessels and nerves, which allowed us to accurately visualize and quantitatively analyze the 3D features of the intact acupoints (Supplementary Fig. 1). We chose CUBIC rather than

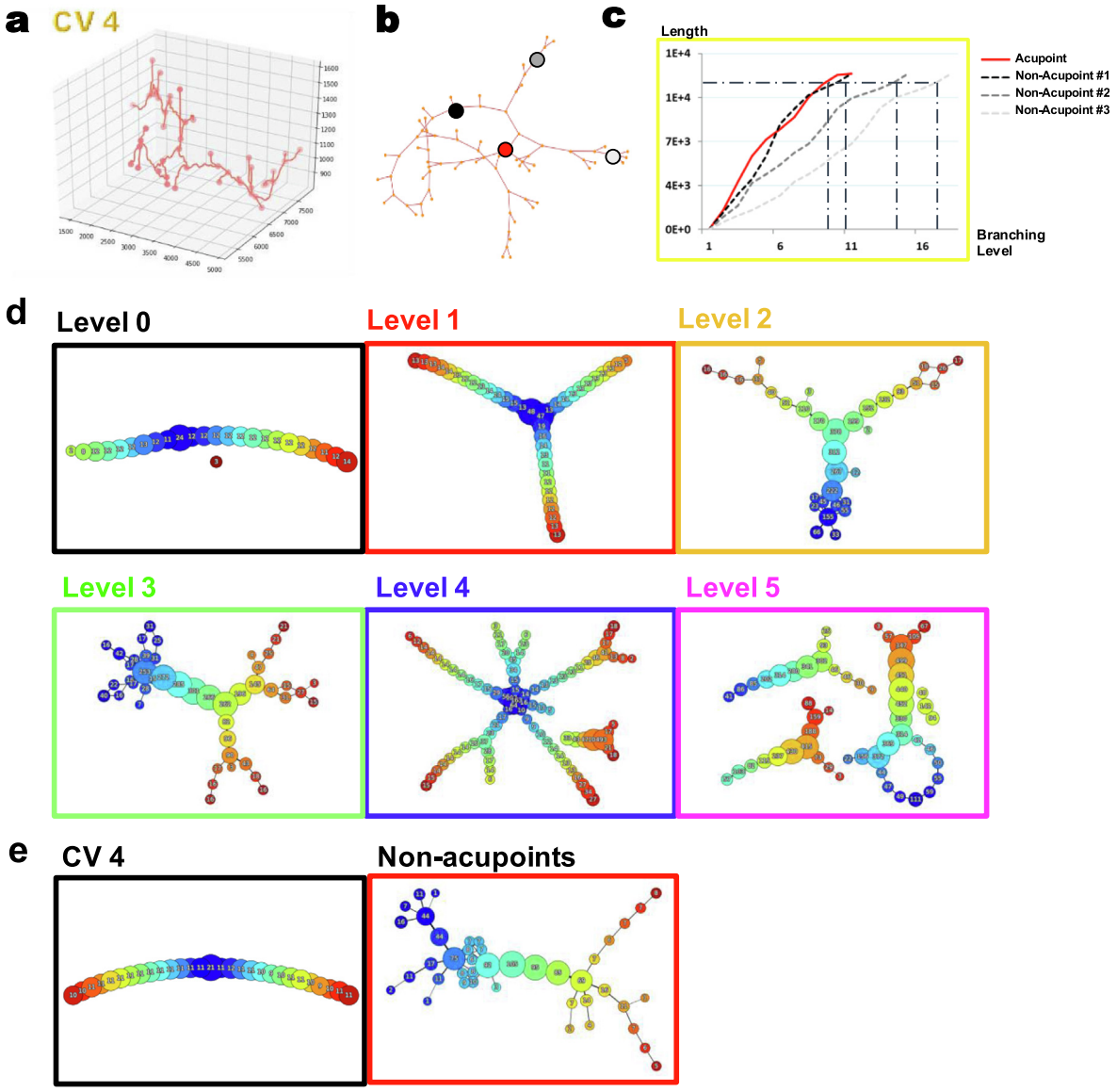

Fig. 4. Topological analysis of the neurovascular 3D structure of acupoints and non-acupoints from a representative mouse from the control group. a). 3D view of the vascular structure of CV 4. b). Tracing of the topological skeleton centered in CV 4. (Red, CV 4; white, CV 4-R; gray, CV 4-U; black, CV 4-L) c). Blood vessel length in relation to branching level. At the acupoint, fewer branching points and longer vessel lengths were found. d). Representative levels of branching points found in acupoints and non-acupoints. e). Representative images for different *Mapper* analyses comparing non-acupoints with CV 4. The number on the node shows the amount of contained data. (For interpretation of the references to color in this figure legend, the reader is referred to the web version of this article.)

CLARITY that we used in previous work because of the shorter clearing time (3 days *vs* 42 days) and the better clearing efficiency [45]. Although acupoints have been assumed to have different structural bases, we did not find any significant differences in the density, diameter, branching level, or sympathetic neurovascular networks between CV 3, 4, 5, and 7 (Supplementary Fig. 2). In addition, no obvious difference was found in 3D neurovascular structures before and after single 30 min EA (Supplementary Fig. 3).

Topological methods are powerful tools for analyzing large genomic datasets, and their application has led to important biological results in the fields of evolutionary biology, cancer genomics, and complex diseases [46]. The biggest advantage of *Mapper* used in our present research was to handle high dimensional data and reveal its topological features when compared with traditional mathematical methods. Furthermore, when compared with other topological methods, *Mapper* could preserve continuous variations and small-scale similarities among data points by using different adapted filters [47]. Using *Mapper*, the sympathetic neurovascular network could be classified into different levels, in which the lower level possessed fewer branching points and thus had better transmission efficacy [36,37]. Interestingly, the sympathetic neurovascular network of the CV 4 acupoint was revealed to be at a lower level compared with the surrounding non-acupoints (Fig. 4e), suggesting its better blood flow and neural signal transmission ability.

Furthermore, we indirectly explored the signal transmission ability of sympathetic neurovascular networks *in vivo*. One common local physiological change induced by MA/EA is the redness of the skin, which is suggested to be related to increased blood flow under the regulation of sympathetic nerves [48–50]. Here we took advantage of the deep light-penetration and high spatial–tem poral-resolution of NIR-II imaging, thus precisely observing blood

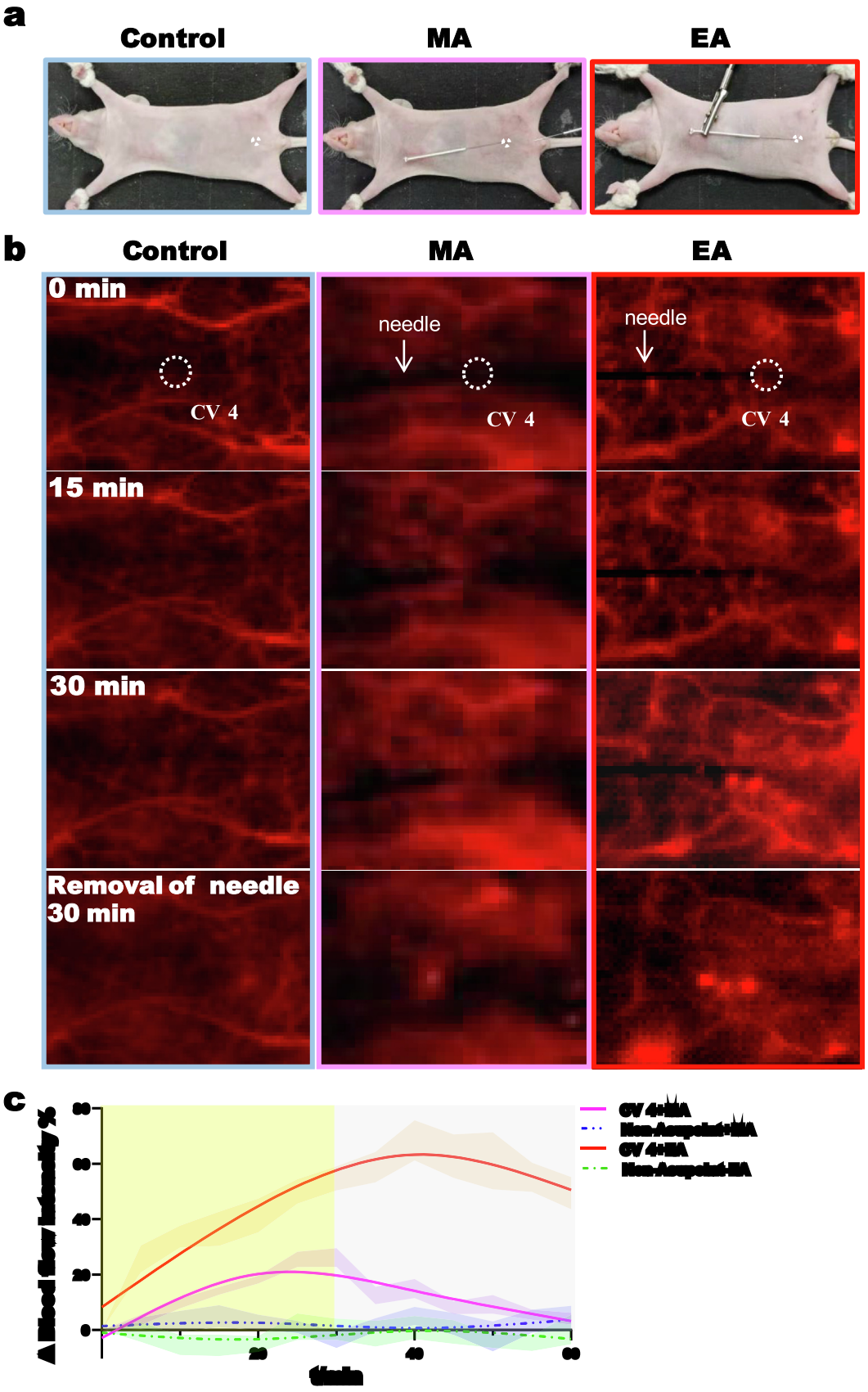

Fig. 5. NIR-II real-time imaging of blood flow in CV 4 and surrounding non-acupoints. a). Nude mice underwent control, MA, and EA treatment at CV 4. b). Blood flow monitoring during the 30 min MA or EA treatment and for 30 min after removal of the needle. The dotted circle indicates the CV 4 region. c). Restricted cubic spline curves of the real-time blood flow changes in CV 4 and non-acupoints at different times after MA or EA treatment. n = 6/group.

flow changes in the CV 4 acupoint and surrounding non-acupoints [51–54]. In addition to previous findings of EA-induced local blood flow [55], we distinguished the CV 4 acupoint and non-acupoint more precisely and found rare blood flow in the surrounding non-acupoints after EA in the CV 4 (Fig. 5c). We used MA in our present research as sham EA, and MA induced weaker and shorter-lasting blood flow suggesting that even slight stimulation of the CV 4 acupoint can lead to a certain degree of increased blood flow.

Of course, the limited number of specimens, the lack of human specimens, and the difficulties of 3D imaging *in vivo* are limitations of this research and need to be further improved.

16. Conclusion

Denser sympathetic neurovascular networks were identified as 3D architectural features of the CV 4 acupoint. Further topological analysis revealed its advanced blood-flow and sympathetic-neural signal transmission ability, and NIR-II revealed increased blood flow in the CV 4 acupoint but not in the surrounding non-acupoints as a result of EA.

Author contributions

Y.F., W.H., A.J.W.H., J.C., and Z.L. conceived the experiments, designed the project and protocols, and developed the collaborations. W.H., X.T., C.S., W.L. Z.J., Y.X, Z.P., M.X., X.X., J.S., Y.L., H.C., Y.L., Y.Y., H.G., and K.O. performed the experiments. W.H, C.S., X. T., and J.C. analyzed the data. W.H, A.J.W.H., J.C., and Y.F. wrote the manuscript. A.J.W.H., F.Z., Z.L., and K.D. provided scientific oversight and guidance and edited the manuscript. W.H., J.C., and Y.F. are the guarantors of this work and, as such, had full access to all of the data in the study and take responsibility for the integrity of the data and the accuracy of the data analysis.

Financial support and sponsorship

This work was supported by the National Natural Science Foundation of China (NSFC 81673766 & 81973945 to Y.F.), the Innovative Research Team of High-level Local Universities in Shanghai, and the Development Project of Shanghai Peak Disciplines-Integrated Chinese and Western Medicine (20180101 to Y.F.), and the Project Supported by Shanghai Municipal Science and Technology Major Project (No.2018SHZDZX01) and ZJLab.

Declaration of Competing Interest

The authors declare that they have no known competing financial interests or personal relationships that could have appeared to influence the work reported in this paper.

Acknowledgments

Wei Hu, Junda Chen, Caixia Sun contributed equally to this work. We thank Ying Shi and Min Jiang of Core Facility of Institute of Brain Science, Fudan University. We thank Jie Wu of Shandong University. We thank Brian Hsueh, Ailey Crow, Kristin Overton, and Karl Deisseroth of Stanford University for helpful discussions and technological support.

Appendix A. Supplementary data

Supplementary data to this article can be found online at https://doi.org/10.1016/j.csbj.2021.04.010.

References

[1] Lee MS, Lee Y-H, Shin B-C, Jeong D-M, Kim MK, Eo Y-G, et al. Is there any energy transfer during acupuncture?. Am J Chin Med 2005;33(03):507–12.
[2] Lim S. WHO Standard Acupuncture Point Locations J Evid-Based Complementary Alternative Med. 2010; 7: 167-8..
[3] Lightbody S. The 361 Classical Acupuncture Points. WORLD SCIENTIFIC; 2018.
[4] Zhou J, Qu F. Treating gynaecological disorders with traditional Chinese medicine: a review. J African J Traditional Complementary Alternative Med 2009;6(4). https://doi.org/10.4314/ajtcam.v6i4.57181.
[5] Huang D-M, Huang G-Y, Lu F-e, Stefan D, Andreas N, Robert G. Acupuncture for infertility: is it an effective therapy?. Chin J Integr Med 2011;17(5):386–95.
[6] Shetty GB, Shetty B, Mooventhan A. Efficacy of acupuncture in the management of primary dysmenorrhea: a randomized controlled trial. J Acupuncture Meridian Stud 2018;11(4):153–8.
[7] Shi Y, Li L, Zhou J, Sun J, Chen L, Zhao J, et al. Efficacy of electroacupuncture in regulating the imbalance of AMH and FSH to improve follicle development and hyperandrogenism in PCOS rats. Biomed Pharmacother 2019;113:108687. https://doi.org/10.1016/j.biopha.2019.108687.
[8] Chen Y, Fang Y, Yang J, Wang F, Wang Y, Yang Li. Effect of acupuncture on premature ovarian failure: a pilot study. Evidence-based complementary and alternative medicine: eCAM 2014;2014:1–6.
[9] Chen S, Sun H, Xu H, Zhang Y, Wang H. Effects of acupuncture on hospitalized patients with urinary retention. Evidence-based Complementary and Alternative Medicine: eCAM 2020;2020:1–7.
[10] Robinson NG. Interactive medical acupuncture anatomy. CRC Press; 2016.
[11] Ifrim-Chen F, Ifrim M. The relation between the acupoint structures and the clinical therapeutic effects. J Italian J Anatomy Embryol 2005;110: 45–9.
[12] Liu S, Wang Z-F, Su Y-S, Ray RS, Jing X-H, Wang Y-Q, et al. Somatotopic organization and intensity dependence in driving distinct NPY-expressing sympathetic pathways by electroacupuncture. Neuron 2020;108(3):436–450. e7.
[13] Liu Z, Wang L, Zhou Z, Sun Y, Wang M, Wang H, et al. The simple neuroendocrine-immune regulatory network in oyster Crassostrea gigas mediates complex functions. Sci Rep 2016;6(1). https://doi.org/10.1038/srep26396.
[14] Ding SS, Hong SH, Wang C, Guo Y, Wang ZK, Xu Y. Acupuncture modulates the neuro–endocrine–immune network. QJM Int J Med 2014;107(5):341–5.
[15] Li N-C, Li M-Y, Chen B, Guo Y. A new perspective of acupuncture: the interaction among three networks leads to neutralization. Evidence-based Complementary and Alternative Medicine: eCAM 2019;2019:2326867-.
[16] Chenglin L, Xiaohua W, Hua Xu, Fang L, Ruishan D, Dongming Z, et al. X-ray phase-contrast CT imaging of the acupoints based on synchrotron radiation. J Electron Spectrosc Relat Phenom 2014;196:80–4.
[17] Zhang D, Yan X, Zhang X, Liu C, Dang R, Xiao T, et al. Synchrotron radiation phase-contrast X-ray CT imaging of acupuncture points. Anal Bioanal Chem 2011;401(3):803–8.
[18] Fu H. What is the material base of acupuncture? The nerves!. Med Hypotheses 2000;54(3):358–9.
[19] Chen L-Z, Kan Yu, Zhang Z-Y, Wang Y-L, Zhang X-N, Wang X-Y, et al. Neuropeptide initiated mast cell activation by transcutaneous electrical acupoint stimulation of acupoint LI4 in rats. Sci Rep 2018;8(1). https://doi.org/10.1038/s41598-018-32048-3.
[20] Mingfu L, Xiaotong D, Xiaojing S, Jin J, Jinling Z, Ying H. Study on the dynamic compound structure composed of mast cells, blood vessels, and nerves in rat acupoint %J. Evidence-Based Complementary and Alternative Medicine 2013;2013:1–4.
[21] Li NC, Li MY, Chen B, Guo Y. A new perspective of acupuncture: the interaction among three networks leads to neutralization. Evidence-based Complementary and Alternative Medicine: eCAM 2019;2019:2326867.
[22] Yin CS, Jeong H-S, Park H-J, Baik Y, Yoon M-H, Choi C-B, et al. A proposed transpositional acupoint system in a mouse and rat model. Res Vet Sci 2008;84 (2):159–65.
[23] Robinson NG. One Medicine. One Acupuncture. J Animals 2012;2(3):395–414.
[24] Chung K, Deisseroth K. CLARITY for mapping the nervous system. Nat Methods 2013;10(6):508–13.
[25] Jing D, Zhang S, Luo W, Gao X, Men Yi, Ma C, et al. Tissue clearing of both hard and soft tissue organs with the PEGASOS method. Cell Res 2018;28 (8):803–18.
[26] Cai R, Pan C, Ghasemigharagoz A, Todorov MI, Förstera B, Zhao S, et al. Panoptic imaging of transparent mice reveals whole-body neuronal projections and skull-meninges connections. Nat Neurosci 2019;22(2):317–27.
[27] Hong G, Antaris AL, Dai H. Near-infrared fluorophores for biomedical imaging. Nat Biomed Eng 2017;1:0010.
[28] Wang S, Fan Y, Li D, Sun C, Lei Z, Lu L, et al. Anti-quenching NIR-II molecular fluorophores for in vivo high-contrast imaging and pH sensing. Nat Commun 2019;10(1). https://doi.org/10.1038/s41467-019-09043-x.
[29] Sun C, Li B, Zhao M, Wang S, Lei Z, Lu L, et al. J-aggregates of cyanine dye for NIR-II in vivo dynamic vascular imaging beyond 1500 nm. J Am Chem Soc 2019;141(49):19221–5.
[30] Ahn AC, Martinsen ØG. Electrical characterization of acupuncture points: technical issues and challenges. J Altern Complement Med 2007;13 (8):817–24.
[31] Lin W. Experimental Acupuncture: Shanghai College of Traditional Chinese Medicine Press; 1989..

[32] Susaki EA, Tainaka K, Perrin D, Yukinaga H, Kuno A, Ueda HR. Advanced CUBIC protocols for whole-brain and whole-body clearing and imaging. Nat Protoc 2015;10(11):1709–27.
[33] Singh G, Mémoli F, Carlsson GE. Topological methods for the analysis of high dimensional data sets and 3d object recognition. J SPBG 2007;91:100.
[34] Li B, Zhao M, Feng L, Dou C, Ding S, Zhou G, et al. Organic NIR-II molecule with long blood half-life for in vivo dynamic vascular imaging. Nat Commun 2020;11(1). https://doi.org/10.1038/s41467-020-16924-z.
[35] Souza VR, Mendes E, Casaro M, Antiorio A, Oliveira FA, Ferreira CM. Description of ovariectomy protocol in mice. Methods Mol Biol (Clifton, NJ). 2019;1916:303–9.
[36] Yemane PT, Åslund AKO, Snipstad S, Bjørkøy A, Grendstad K, Berg S, et al. Effect of ultrasound on the vasculature and extravasation of nanoscale particles imaged in real time. Ultrasound Med Biol 2019;45(11):3028–41.
[37] Kloosterman A, Hierck B, Westerweel J, Poelma C, Secomb TW. Quantification of blood flow and topology in developing vascular networks. J PloS One 2014;9(5):e96856.
[38] Meng X, Guo X, Zhang J, Moriya J, Kobayashi J, Yamaguchi R, et al. Acupuncture on ST36, CV4 and KI1 suppresses the progression of methionine- and choline-deficient diet-induced nonalcoholic fatty liver disease in mice. Metabolites 2019;9(12):299. https://doi.org/10.3390/metabo9120299.
[39] Chang S. The meridian system and mechanism of acupuncture—a comparative review. Part 1: The meridian system. Taiwanese J Obstetrics Gynecol 2012;51:506–14.
[40] Longhurst JC. Defining meridians: a modern basis of understanding. J Acupuncture Meridian Stud 2010;3(2):67–74.
[41] Zhou F, Huang D, YingXia. Neuroanatomic Basis of Acupuncture Points. In: Xia Y, Cao X, Wu G, Cheng J, editors. Acupuncture Therapy for Neurological Diseases. Berlin, Heidelberg: Springer Berlin Heidelberg; 2010. p. 32-80..
[42] Li Q-Q, Shi G-X, Xu Q, Wang J, Liu C-Z, Wang L-P. Acupuncture effect and central autonomic regulation. Evidence-based Complementary and Alternative Medicine: eCAM 2013;2013:267959-.
[43] Luo T, Guo Yi. Specificity study on concentration of monoamine transmitters at acupoint and effect of acupuncture on its distribution. Evidence-based Complementary and Alternative Medicine: eCAM 2014;2014:1–5.
[44] Chen S, Wang S, Rong P, Wang J, Qiao L, Feng X, et al. Acupuncture for visceral pain: neural substrates and potential mechanisms. Evidence-Based Complementary and Alternative Medicine. 2014;2014:1–12.
[45] Zhang WL, Liu SH, Zhang WC, Hu W, Jiang M, Tamadon A, et al. Skeletal muscle CLARITY: a preliminary study of imaging the three-dimensional architecture of blood vessels and neurons. Cell J 2018;20:132–7.
[46] Cámara PG. Topological methods for genomics: present and future directions. Curr Opin Syst Biol. 2017;1:95–101.
[47] Wang T, Johnson T, Zhang J, Huang K. Topological methods for visualization and analysis of high dimensional single-cell RNA sequencing data. Pac Symp Biocomput. 2019;24:350–61.
[48] Li W, Ahn A. Effect of acupuncture manipulations at LI4 or LI11 on blood flow and skin temperature. J Acupuncture Meridian Stud 2016;9(3):128–33.
[49] Sheng Y, Zhu L. The crosstalk between autonomic nervous system and blood vessels. Int J Physiol Pathophysiol Pharmacol. 2018;10:17–28.
[50] Tamai K, Imai K, Hisajima T. Effects of cathode direct-current electroacupuncture stimulus of the promixal anterior lower limbs on heart rate and lumbar blood flow. Med Acupunct 2020;32(2):71–9.
[51] Hong G, Lee JC, Robinson JT, Raaz U, Xie L, Huang NF, et al. Multifunctional in vivo vascular imaging using near-infrared II fluorescence. J Nature Med 2012;18(12):1841–6.
[52] Gómez-Gaviro MV, Balaban E, Bocancea D, Lorrio MT, Pompeiano M, Desco M, et al. Optimized CUBIC protocol for three-dimensional imaging of chicken embryos at single-cell resolution. Development 2017;144(11):2092–7.
[53] Nehrhoff I, Bocancea D, Vaquero J, Vaquero JJ, Ripoll J, Desco M, et al. 3D imaging in CUBIC-cleared mouse heart tissue: going deeper. Biomed Opt Express 2016;7(9):3716–20.
[54] Feng Yi, Zhu S, Antaris AL, Chen H, Xiao Y, Lu X, et al. Live imaging of follicle stimulating hormone receptors in gonads and bones using near infrared II fluorophore. J Chem Sci 2017;8(5):3703–11.
[55] Kim S-Y, Min S, Lee H, Cheon S, Zhang X, Park J-Y, et al. Changes of local blood flow in response to acupuncture stimulation: a systematic review. Evidence-based Complementary and Alternative Medicine: eCAM. 2016;2016:1–11.